ELSEVIER

Contents lists available at ScienceDirect

Measurement

journal homepage: www.elsevier.com/locate/measurement





Evaluating the precision and reproducibility of non-invasive deformation measurements in an arterial phantom

Aleksander Sinek ^{a,b}, Mateusz Mesek ^{a,b}, Marek Rojczyk ^a, Jan Juszczyk ^c, Wojciech P. Adamczyk ^{a,*}, Jacob Sturdy ^b, Bartłomiej Melka ^a, Adam Golda ^d, Michał Nowok ^d, Ziemowit Ostrowski ^a, Ryszard Białecki ^a

- ^a Silesian University of Technology, Department of Thermal Technology, biomed~^{lab}, Biomedical Engineering Lab, Konarskiego 22, 44-100 Gliwice, Poland
- b Norwegian University of Science and Technology, Department of Structural Engineering, Richard Birkelands vei 1A, Trondheim 7034, Norway
- ^c Silesian University of Technology, Faculty of Biomedical Engineering, Department of Medical Informatics and Artificial Intelligence, Roosevelta 40, 41-800 Zahrze, Poland
- ^d Gliwice Municipal Hospital No. 4, Cardiology Ward, Kosciuszki 29, 44-100 Gliwice, Poland

ARTICLE INFO

Keywords: Image processing Fluid-structure interaction Linear mixed-effects modeling Error analysis Ultrasound Pulsatile flow

ABSTRACT

Computer modeling combined with non-invasive measurement modalities may provide a means to advanced diagnosis and treatment of cardiovascular diseases; however, development and validation of novel methods is often impeded by the challenge of gathering relevant clinical data. We present an experimental rig and phantom model of the left common carotid artery developed to generate data necessary for the validation of a computational model of the artery. The flow rates and pressures at the inlet and outlet, and deformation of the phantom were measured simultaneously with optical and ultrasound systems. A statistical analysis of the precision and reproducibility of the measurements found experiment-to-experiment variations were less than 3.1 mmHg, 0.023 L/min, and 0.012 mm for pressure, flow and displacement respectively. The mean difference between ultrasound measured displacement and camera measured displacement was 0.0113 mm.

1. Introduction

Every 40 s someone suffers a stroke in the United States, typically without a specific warning, and every 3.5 min a stroke leads to death [1]. Cardiovascular diseases, including strokes, are the leading cause of death and often substantially impair quality of life, and with current trends in aging and disease the total burden of these diseases is expected to grow substantially [2,3]. Many cardiovascular diseases present symptoms only after the disease has progressed well beyond its initial pathology. The increased burden of cardiovascular disease in the population, the difficulty of early diagnosis, and the complexity of the regulation and function of the cardiovascular system call for improved methods to assess the cardiovascular system without substantial increase in clinical burden. Research efforts have improved understanding of many aspects of cardiovascular physiology and disease progression. Based on this understanding properties of the cardiovascular system like arterial stiffness have been established as predictors of cardiovascular risk [3], but routine assessment and monitoring of detailed properties of the cardiovascular system is impeded by the limited opportunity of collecting direct measurement of tissues and physical state in the arteries of healthy and diseased individuals. This

in turn limits diagnosis of disease and monitoring of treatment effects. Various imaging modalities and non-invasive sensors for pressure and flow have been highly effective in clinical applications, but validation of their performance when used to indirectly estimate properties such as arterial stiffness requires direct measurements through highly invasive and possibly destructive procedures. Laboratory phantoms provide a useful means of replicating non-invasive methods in a context where direct corroboration of results is straightforward [4–8].

A number of methods have been developed for quantification of large artery stiffness, and most focus on estimating the Pulse Wave Velocity (PWV). These include highly invasive (pressure catheters), noninvasive (carotid-femoral tonometry) and indirect (single cuff) methods. While inexpensive and commonplace, PWV methods are best suited for estimating arterial stiffness in larger vessels (most often aorta) over a region [9]. Particularly, the current "gold standard" in regional PWV-based measurements is the carotid-femoral technique, but it has limited diagnostic power due to lack of indication of local variations in stiffness along the arterial tree and a somewhat arbitrary definition of the carotid-femoral distance [10]. The importance of local

E-mail address: wojciech.adamczyk@polsl.pl (W.P. Adamczyk).

^{*} Corresponding author.

measurement is further highlighted by the fact that early stages of atherosclerotic diseases (associated with arterial stiffness) only affect elastic properties of arteries locally and may be missed by a regional approach [11]. Even though there are novel approaches developed for estimating local stiffness (e.g. Shear Wave Elastography or loop-based methods [9]), there is not yet an agreed upon 'gold standard'.

We propose a method for estimating arterial stiffness that is not based on PWV, but rather is based solely on the displacements of the artery itself. Development, validation, and implementation of such method require access to data. Laboratory phantoms serve as a low risk and economical environment for this task. In this article we present an experimental set-up that was designed to test whether the proposed approach is feasible and to generate data that will further serve the development of the displacement-based method. To better reflect the target clinical application, physiological flow conditions of the human common carotid artery were reproduced [12] and many modifications to the experimental set-up, common in the literature, were implemented (e.g. hydraulic capacitor to mimic the 'cushioning' role of the aorta) [13,14]. The focal point of the rig is the carotid arterial phantom, which undergoes periodic displacements that are subsequently captured by both optical cameras and an ultrasound system. We performed a series of experiments using this testing rig with the aim of accurately capturing the displacements of the carotid phantom.

Short measurement times, ease of operation and affordability have lead to frequent use of ultrasound for PWV-based assessment of arterial stiffness [15], however, few studies report on direct measurement of displacements with ultrasound systems, and even fewer quantify the accuracy or benchmark against more established methods for measuring displacements [16]. To address this issue, high-speed cameras were chosen for comparison with the ultrasound system due to their prevalence in literature and relatively low bias [17].

This article begins with an overview of the experimental rig and describes briefly the equipment used, the sampling rate and the Data Acquisition procedure for both the rig and the ultrasound system. Performed measurements resulted in flow, pressure, camera, and ultrasound data that were first processed using scripts developed in-house and subsequently subjected to statistical analysis. The purpose of the analysis was to assess the repeatability of performed experiments and to comment on the similarity (or lack thereof) between the displacements registered using ultrasound and digital cameras. With this information, we were able to comment on the use of ultrasound for capturing the displacements of artery phantoms, which is a crucial first step in the development of the non-invasive technique for displacement-based estimation of local arterial stiffness of actual humans [18].

2. Experimental facility

The experimental test rig is presented schematically in Fig. 1, and a photograph of the real configuration is shown in Fig. 2. The experimental rig was designed to simulate the behavior of the Left Common Carotid Artery (LCCA) and to allow direct monitoring the deformation of a distensible pipe exposed to the simulated cardiac pressure and flow cycle. The volumetric flow rate was held around $0.5\ l/min$ to simulate physiological conditions in the LCCA of an adult male [19]. To collect a wide range of data while working with limited resources, measurements were carried out over a series of four systole/diastole pressure ratios (A) 110/70 mmHg, (B) 120/80 mmHg, (C) 135/95 mmHg and (D) 140/100 mmHg. These four ratios were chosen as they cover a wide range of physiological values and scenarios. They can be classified as: A - optimal, B - normal, C - high normal and D - Grade 1 hypertension [12] To generate the required the flow rate, a Harvard Apparatus Pulsatile Blood Pump dedicated for large animals was used [20] as this pump closely simulates the ventricular action of the heart. For all measurements performed, the stroke volume was set to 15 ml, stroke rate to 60 r.p.m., and the systole/diastole flow ratio to 35%:65%. The working fluid was water, and the flow rate was measured by

an Endress+ Hauser Dosimag electromagnetic flow meter [21] and controlled manually. Eight pressure transducers (Harvard Apparatus Blood Pressure Transducers APT300) together with Compact Transducer Amplifiers (Harvard Apparatus) were installed to measure the pressure at several points proximal and distal to the phantom.

To confirm that the displacement of the tube could be reconstructed from the images of the tube's deformation, the change in external diameter was determined using two high-speed cameras: a Phantom MIRO C110 and a Phantom VEO 710 [22]. The Phantom MIRO C110 recorded 1000 frames per second (FPS) of resolution 1280×900 , which covered 22% of the entire tube. This was achieved by using the irix lens [23] (150 mm f/2.8 Macro 1:1) together with a 20 mm extension tube. The second camera, a Phantom VEO 710 was equipped with a NIKKOR 200 mm F/4.0 MACRO lens with the additional 68 mm extension tube, and recorded 1000 FPS of resolution 1280×800 covering 30% of the tube. The cameras were mounted perpendicularly to one another to capture the tube deformations in two orthogonal directions (see Fig. 2). Finally, two backlights were installed to eliminate background features and sharpen the edges in the images from each camera.

2.1. Ultrasound measurement system

For simultaneous measurement of displacement with ultrasound, only the VEO (side) camera and ultrasound probe were used. The probe and camera were mounted perpendicularly to each other to acquire the same region of the LCCA phantom in both the ultrasound images and the camera and to ensure comparable deformations were recorded. A GE Healthcare Ultrasound Vivid S70N machine with an ML6-15 linear probe was used for recording. The Cardiac preset was used with a modification to allow the ECG signal channel to be used for synchronization. The penetration depth was set to 1.5 cm, and pixel resolution was 0.025 mm per pixel. Image series were recorded over 30–45 s with an acquisition frequency of 59.9 FPS. The LCCA phantom images were captured in the longitudinal plane. For better repeatability the ultrasound probe was fixed during recording using a clamp. During all experiments, the US system imaged the same part of the LCCA phantom.

Ultrasound image time series were recorded simultaneously with high-speed imaging and flow and pressure measurements. For time synchronization of data (flow, pressure, high-speed imaging, and US imaging) an in-house LabVIEW application was used to initiate data collection and to trigger the signal generator (RIGOL) which was connected to the ECG signal input in the US machine (see Fig. 3). The ultrasound system thus recorded the synchronization signal simultaneously with the ultrasound images such that they could be aligned with the other data in post processing. The same pseudo-ECG signal initiated the measurement process of the remaining devices.

2.2. Measurement procedure

The data collection from the experimental rig was controlled by an in-house application written in LabVIEW (National Instruments Corp., USA). This custom application enabled simultaneous acquisition of numerical pressure and flow data from measurement devices. These were collected every 10 ms (100 Hz), while image data was collected every 1 ms (1000 Hz). The high frequency camera recordings enable precise, smooth tracking of the deformation process. To achieve synchronous recording of pressure and flow values every 10 ms, the field programmable gate array (FPGA) implemented in the cRIO 9074 controller was used to read the values from the 8 pressure sensors and 2 flow meters. After the data are read by the FPGA, each of the measured quantities is sent as a vector to the real-time (RT) loop through direct memory access (DMA FIFO). The RT loop collects all vectors as a matrix and every 500 ms sends a matrix from RT to the host (local PC) where the data is saved to a file. (See inset of Fig. 3 for an overview of the data flow).

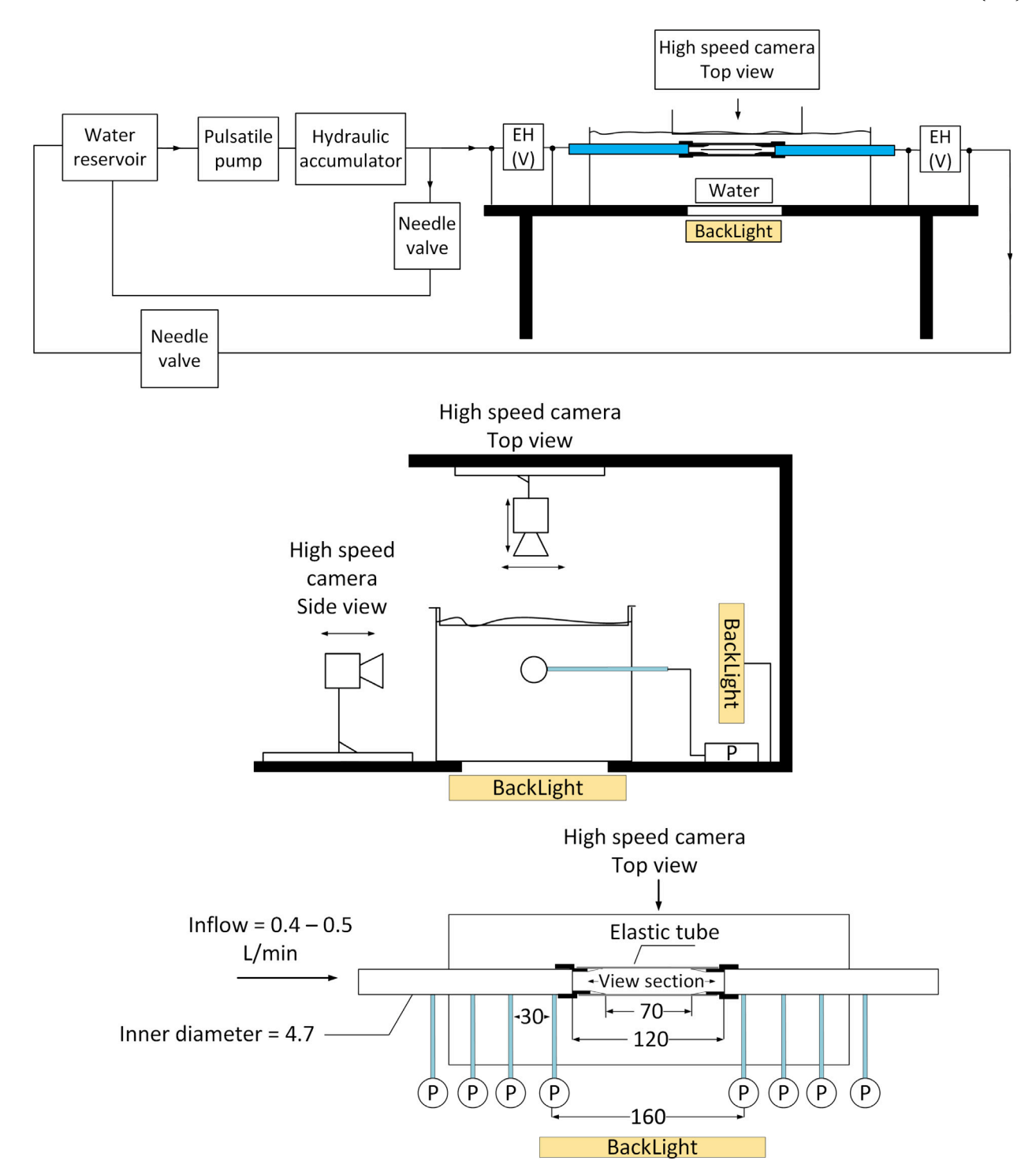


Fig. 1. Scheme of the entire testing rig. EH is the Endress Hauser electromagnetic flow meter, side view and detailed schematic of the distensible tube with locations of the pressure gauges P. Units which are suppressed from the scheme are in millimeters.

The calibration for the Dosimag flowmeters was carried out by the hardware suppliers, and verified by connecting the electromagnetic Dosimage flowmeters in series with a turbine flowmeter (KOBOLD) [24]. Then different volumetric flow rates were imposed in the test line, and the measurements from the flowmeters were compared to verify that all flowmeters produced concurrent measurements over a range of flow rates. The calibration of pressure transducers and Compact Transducer Amplifiers (CTAs) was achieved by isolating the region of the rig where the transducers were located into a closed loop to which a column of liquid was connected. Two calibration points were selected according to the manufacturer's manual [25]; 0 mmHg gauge pressure

(corresponding to 0 V signal from transducers) and 100 mmHg gauge pressure (corresponding to 1 V, giving 100 mmHg/1 V ratio). The pressure was controlled by the height of a liquid column. At 0 mmHg and 100 mmHg the low and high values of the CTAs were adjusted to correctly capture the applied pressure.

To ensure synchronization of the recorded images with pressure and flow waveforms, a dedicated procedure was programmed into the control application. Once the flow and pressure were calibrated to the desired level, data recording was initiated manually, and the control system triggered the cameras to begin recording at detection of the first subsequent decreasing trend in volumetric flow. Both cameras then

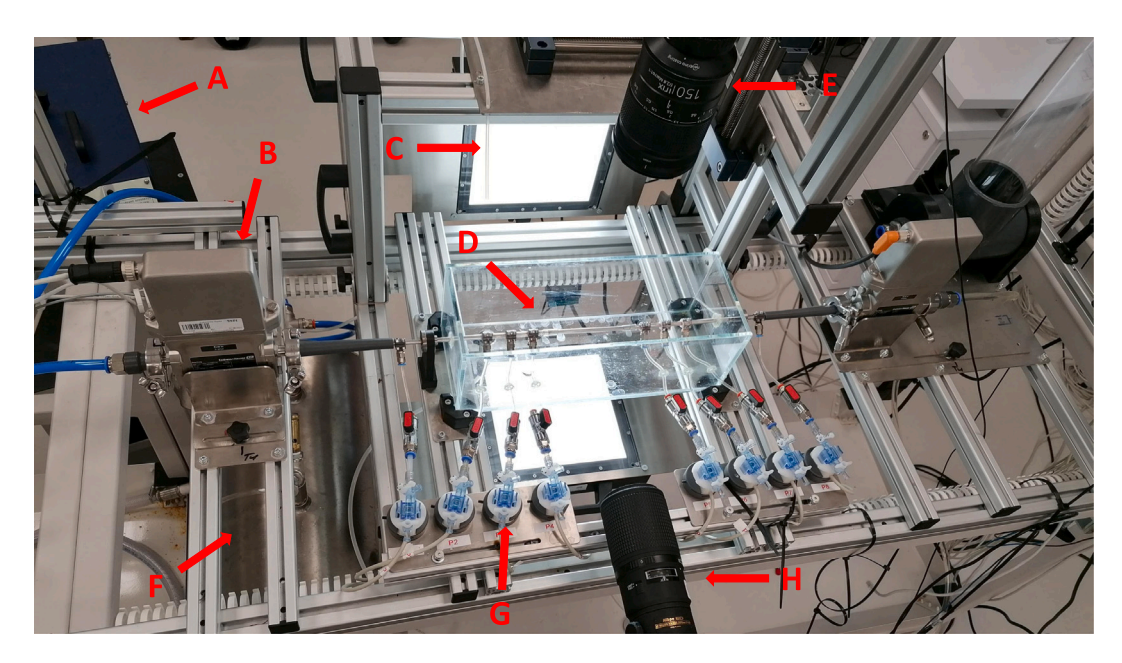


Fig. 2. Configuration of the test rig with devices used for data acquisition with arrows indicating various elements of the set-up. A - periodic pump, B - flowmeter, C - backlight, D - arterial phantom, E - top camera (MIRO), F - reservoir tank, G - pressure transducers, H - side camera (VEO).

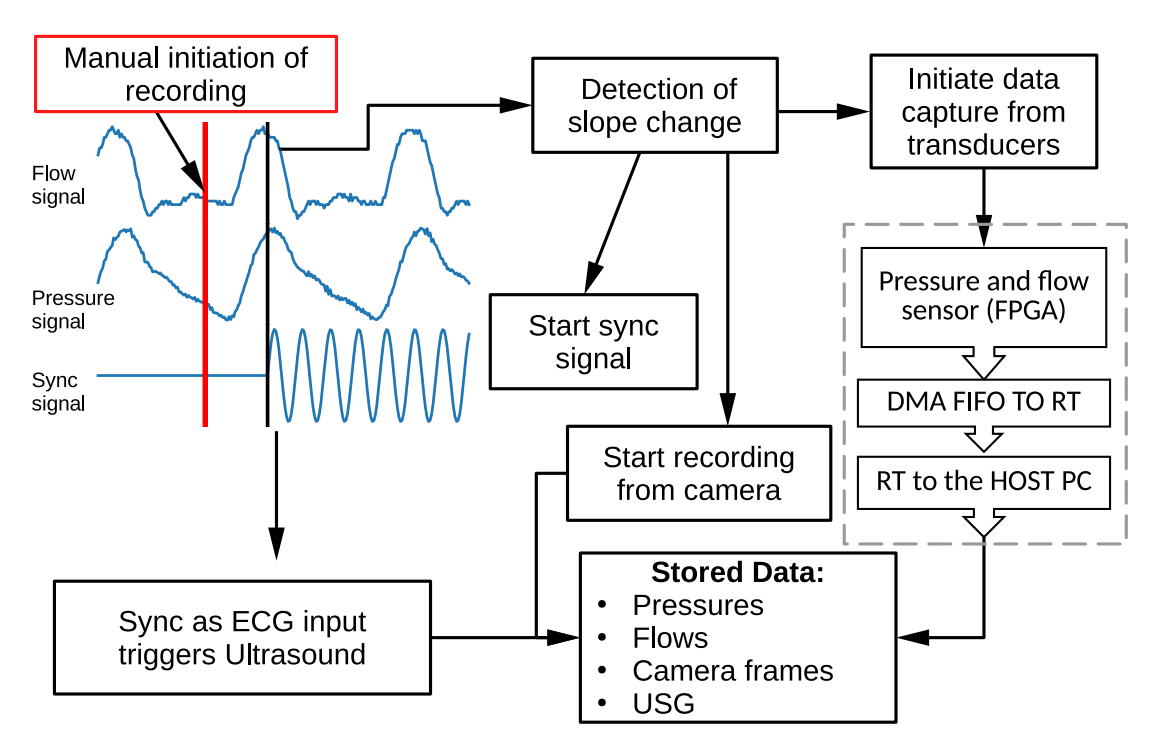


Fig. 3. The initiation and synchronization of data acquisition across transducers, cameras and the ultrasound system is illustrated schematically. First, once conditions are stabilized a manual trigger is sent (red vertical line) after which the signal from the flowmeter is monitored. When the decreasing trend in flow is detected (black vertical line) data collection begins, and a synchronization signal is generated and sent to the ultrasound system. The inset with dashed lines illustrates the programming of the FPGA to read pressure and flow data every 10 ms. These values are received by an RT loop in the controller and stored in memory, and subsequently the values are read from this memory to the host PC where they are collected in a data file.

recorded images for 5 s. This allowed recording a few pump cycles yielding around 5000 images for both cameras (see Fig. 3).

2.3. Processing of data into cycles

The data from both pressure transducers and flow meters were first processed to remove external noise with a Hampel filter, as it is in general robust towards outliers [26]. After this initial pre-processing, the data were split into individual cycles in order to average each

point of the cardiac cycle over time. This was achieved by employing a simple minima-seeking algorithm to identify the start point of each cycle. Starting from the beginning of the data the algorithm would seek out minima by moving through the pressure and displacement data with a fixed step, t_{step} , and then looking for the minimum in a fixed window, $(t_{step} - w, t_{step} + w)$, where w was a constant determining window width and t_{step} is the expected cycle length. This algorithm was quite robust for pressure and displacement data (the determination of displacement data is described in Section 3), since their end-cycle

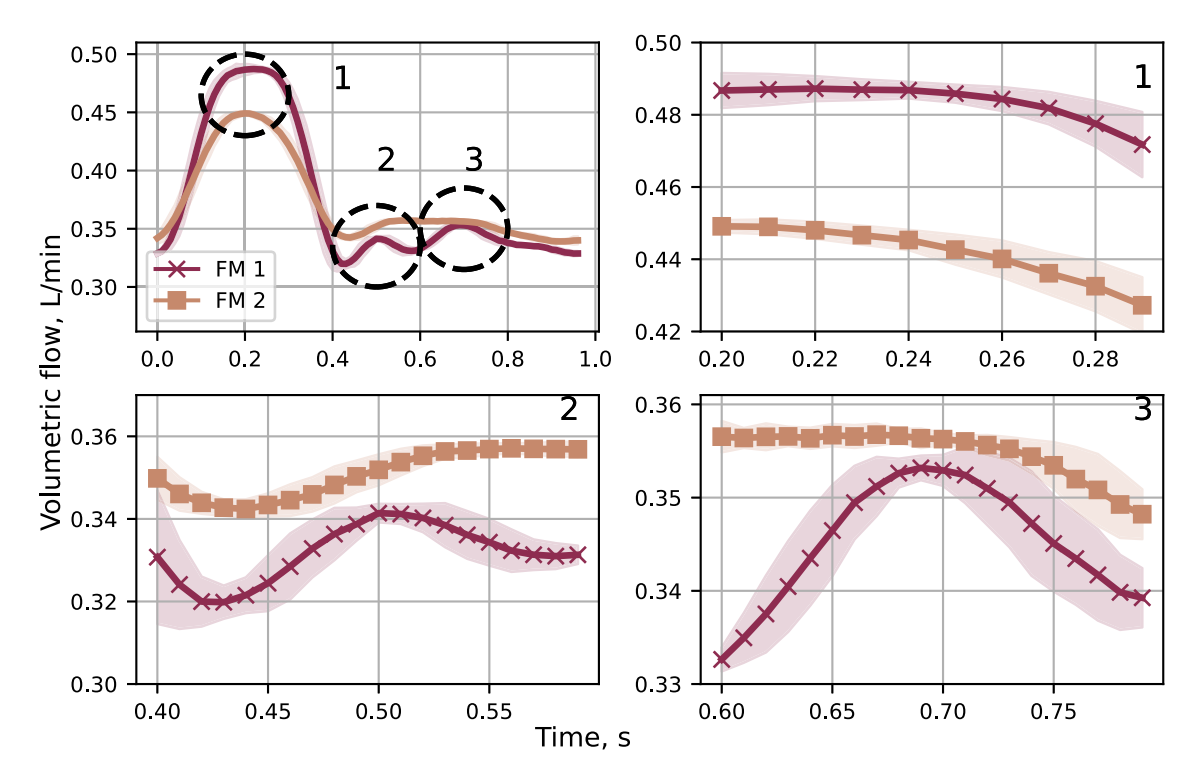


Fig. 4. Time- and measurement-averaged representative flow curves for both flow meters with 95% confidence intervals (top left figure) along with zoomed-in regions, each indicated by a number corresponding to the region in the overall plot.

minima were clearly isolated, it was insufficient for the flow data that exhibited many low amplitude oscillations at the end of each cycle. These impeded automatic determination of the minima corresponding to the end of the cycle. Since pressure and flow data were collected with the same frequency and were expected to have the same duration, power spectrum density [27] of the pressure data was computed to identify the dominant frequency corresponding to the cycle length. This frequency was then used to determine t_{step} , and the width of the window was reduced to avoid splitting cycles due to noise or flow oscillations near the cycle's end.

The experimental procedure was repeated 7 times for each of the four systole/diastole pressure ratios, and a simple statistical procedure was carried out to characterize the variability of the pressure and flow waveforms. Figs. 4 and 5 show the across-time and across-measurement averaged waveforms for both pressure and flow data respectively. In both figures a 95% confidence interval [28] was computed by

$$\mu \in \bar{x} \pm t_{\alpha/2, n-1} \frac{S^2}{\sqrt{n}} \tag{1}$$

where μ is the population mean (true value) for pressure (or flow) values, \bar{x} is the (sample) data mean first calculated across measurement series and then within each averaged measurement, S^2 is the (sample) data variance, $t_{\alpha/2,n-1}$ is the critical value for a two-sided confidence interval based on Student's t-distribution and n is the amount of cycles within a measurement. The resulting confidence intervals for the average waveforms suggest that both pressures and flows were repeatable.

3. Optical camera processing

To determine displacements from the recorded images, an automatic processing algorithm was implemented in Python 3.9 with openCV [29], NumPy [30], SciPy [31] and Pandas [32]. The process is summarized graphically in Fig. 6 where the left branch shows the process for obtaining the diameter of the phantom from a recorded image, and the right branch illustrates how pixel dimensions of each camera were determined.

The raw images from both cameras only record pixel information, thus to extract distances and displacements in millimeters, the linear dimensions of the pixel were determined for both cameras. As both cameras have isotropic pixel dimensions, it is sufficient to determine the dimensions along a single axis. A calibration procedure was carried out at the beginning of each measurement. First, a linear scale suited for microscopy (for high precision) was placed in the same position that the phantom would occupy, and each camera recorded an image of this scale. The images of the scale were filtered to detect edges (see the right branch of Fig. 6). This resulted in a filtered image with a strip of points located on each vertical edge corresponding to the edges of the divisions of the linear scale. The thickness of a single vertical division of the scale is defined by the two edge points $X_{i,left}$ and $X_{i,right}$, which are averaged to obtain the center $X_i = (X_{i,\text{right}} - X_{i,\text{left}})/2$ (red dots in the right branch of Fig. 6). The length, l_{true} , (in millimeters) between the left-most and right-most lines was determined by the division of the microscopic scale (0.5 mm) and the number of division lines captured in the image. The length in pixels, l_{pixels} , covered by the linear scale was calculated as the difference between the average pixel coordinates of the left-most division line and the average coordinates of the rightmost division life. The linear dimension of the pixel was then obtained by dividing the calculated length, $l_{\it true},$ by the distance in pixels. Across all experiments and cases, the median scale fo the MIRO camera was 112.51 (interquartile range 0.19) pixels/mm while for VEO the median scale was 76.75 (interquartile range 0.39) pixels/mm. To verify the calibration procedure, the linear dimensions were also determined with ImageJ (LOCI, University of Wisconsin, [33]) for several test cases and identical results were found.

Displacements were then determined from each image of the phantom recorded during each measurement. The first step was blurring of the image, followed by applying a Canny detection filter (see left branch of 6) with high and low thresholds of 100 and 200 to produce an image with pixel values of 0 everywhere except at the edges of the tube [34]. The distance between the edges was determined by traversing the image vertically at a given horizontal position, X, and storing (X,Y) coordinates of nonzero pixels (red dot in the left branch

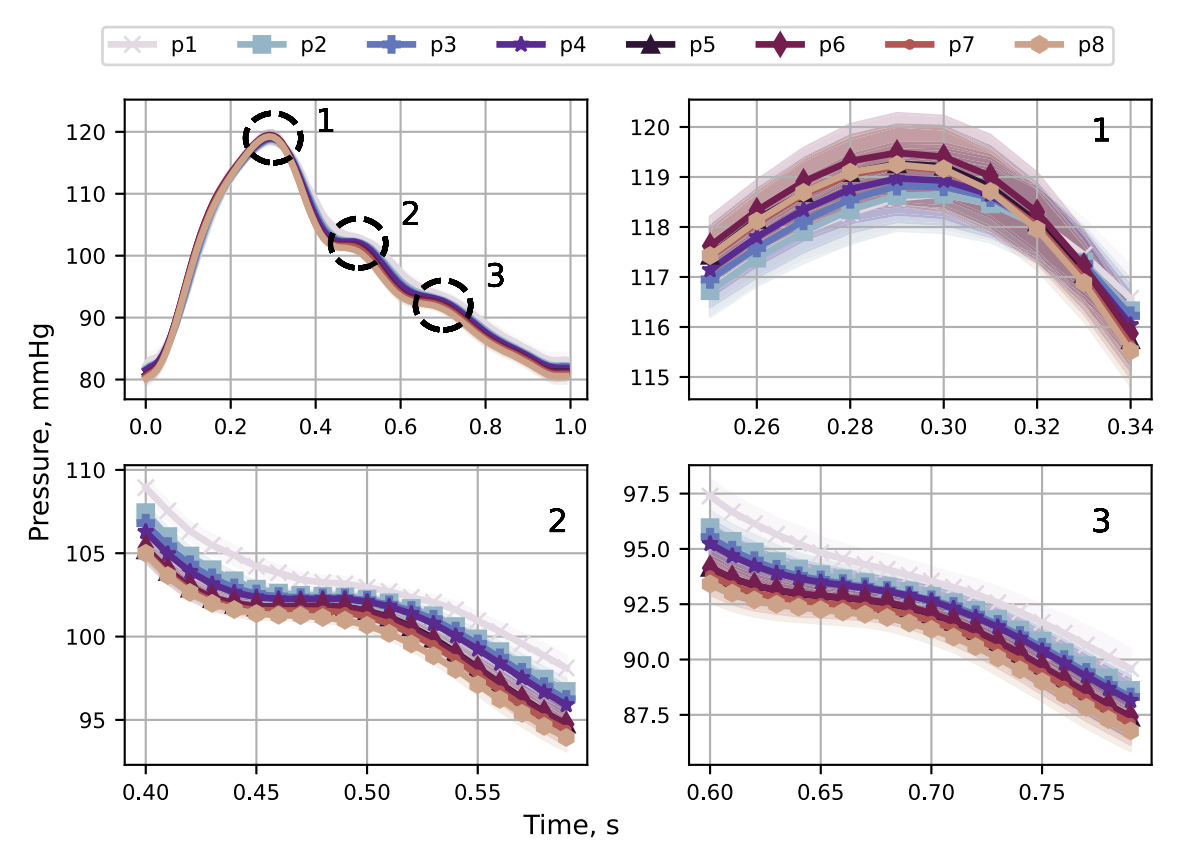


Fig. 5. Time- and measurement-averaged representative pressure curves for all 8 transducers with a 95% confidence interval (top left) along with zoomed-in regions, each indicated by a number corresponding to the region in the overall plot.

of Fig. 6). For a given horizontal position X_1 there were two points, (X_1,Y_1) and (X_1,Y_2) , corresponding to opposite vertical position on the tube $(Y_1$ and $Y_2)$ at some fixed horizontal position (X_1) . Next, the diameter in pixels, d, was calculated as the difference between these two Y coordinates. This process was repeated in the horizontal direction (positive X direction) and for each image yielding diameters at each horizontal location for each time, d(X,t). Then a spatial average was computed $\bar{d}(t) = \frac{1}{N} \sum_X d(X,t)$. Finally, as the main quantity of interest is the displacement, the difference $d_{\rm rel}(t) = \bar{d}(t) - \bar{d}_{\rm diastole}$ is computed and analyzed in the remainder of the work. The diastolic diameter, $\bar{d}_{\rm diastole}$ was defined as the minimum $\bar{d}(t)$ determined over the entire recording.

4. Ultrasound image processing

As the ultrasound system captures images with different characteristics than the optical cameras, a different workflow was employed to process the images from the ultrasound recordings. First, a rectangular region of interest is manually set on the first image in the series such that subsequent analysis of the individual frames is faster, more robust and fully automatic. This process is illustrated in Fig. 7. Due to different gain values for different image series, the image's grayscale values were first normalized (Fig. 7a). Next, the contrast between the wall and lumen of the artery phantom was enhanced by using a morphological operation (Fig. 7b). In the following step, the image was binarized by the Otsu method [35] (Fig. 7c). After this step, the image contains several regions. The largest region indicates the region occupied by the phantom lumen in the original image (Fig. 7d).

The diameter of the phantom was determined from the orthogonal distance between the two boundaries of the lumen mask. As the angle of the phantom relative to the probe varied between ultrasound scans, this angle was determined in order to calculate the cross-sectional diameter. Starting from the phantom lumen mask, the boundaries of

the vessel lumen were identified using the Sobel filter [36] (Fig. 7e). Based on these boundaries, the angle of the upper and bottom edges was determined using the Hough transform [37] (Fig. 7f - green lines). Finally, the phantom's primary angle was defined as the average of the angles of the upper and lower edges of the phantom, which are in general not parallel, and the phantom diameter was computed as the length of the cross-section perpendicular to the phantom's primary angle. For subpixel detection of differences between diastole and systole of the phantom, the phantom's diameter at each perpendicular cross-section was computed and a spatially averaged value tabulated as an estimate of the phantom diameter. For visualization, the LCCA phantom lumen mask was rotated so that the primary angle is parallel to the horizontal axis of the image (Fig. 7g). A representative time series of the phantom's diameter over several cycles is shown in Fig. 8.

5. Mixed effects modeling of waveform data

The experimental procedure was repeated for various experimental specimens and conditions, and data was collected for many cycles in a given experiment. Consequently, the measured data may vary due to factors beyond equipment noise or sensor error. Cycle-to-cycle and experiment-to-experiment variations could be attributed to various uncontrollable factors during experimental set-up such as material fatigue, varied filling of the reservoir or aquarium with artificial artery, etc. To asses the impact of the aforementioned effects, a statistical analysis of the experimental data was conducted. We analyzed the variability of the data between cycles and experiments with a linear mixed modeling approach to partition the variability of the data into components due to residual error, cycle-to-cycle variations and experiment-to-experiment variations. This decomposition is illustrated conceptually in Fig. 9. Pressure, flow or displacement cycles observed in a given configuration are assumed to have essentially identical shapes but may vary up or down from the mean pressure level. Cycles within a given experiment

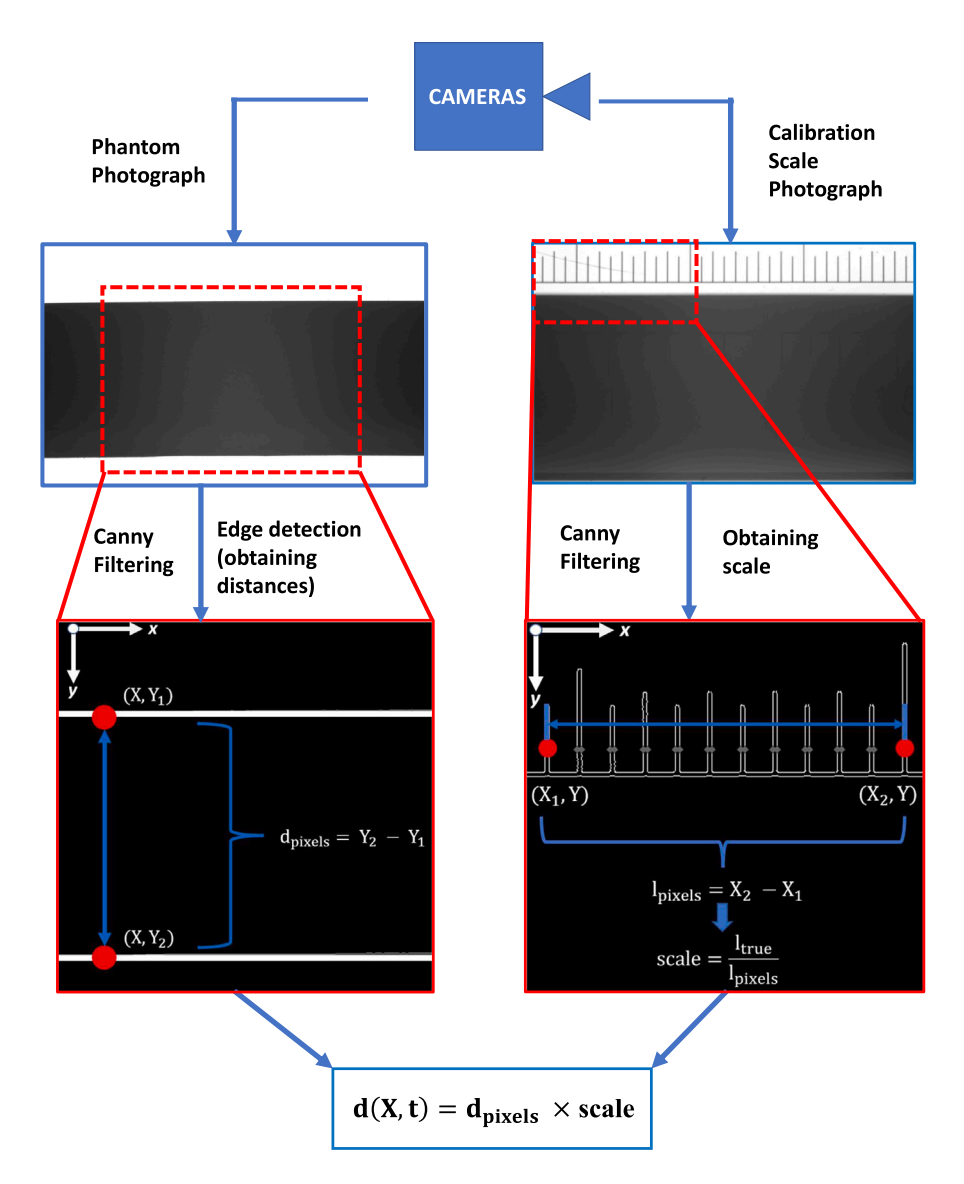


Fig. 6. This figure illustrates the image processing workflow. The left side depicts the determination of diameters from a filtered image. At each column of pixels, X location, the filtered image has two corresponding Y locations. The distance between them (after converting from pixels to millimeters) corresponds to the phantom diameter in pixels. The right side depicts the process of obtaining the conversion factor between pixels and millimeters. Filtering the image of the linear scale yields left and right edges $X_{i,\text{left}}$ and $X_{i,\text{right}}$ at each scale division. The positions of the first and last scale divisions are determined by averaging the position of the divisions' left and right edges, $X_i = X_{i,\text{right}} - X_{i,\text{cirt}} / 2$. Then the distance is calculated as $I_{pixels} = X_2 - X_1$. Subsequently the pixel edge length (millimeters per pixel) was obtained by dividing the true distance by the pixel distance. Finally, the phantom diameter in millimeters is computed given the diameter in pixels and the conversion factor.

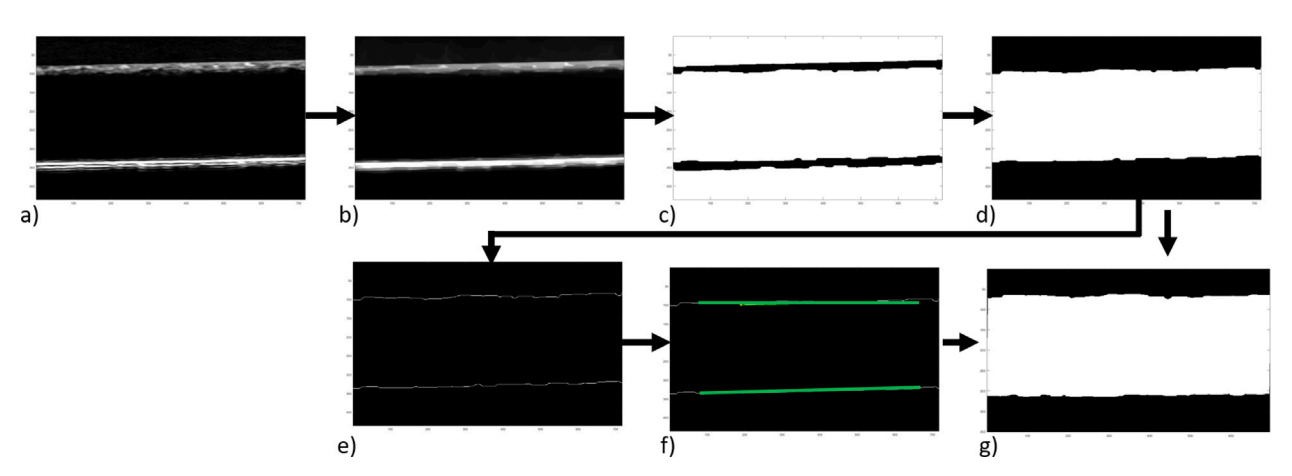


Fig. 7. The workflow for processing ultrasound images, (a) original image, (b) gray scale adjustment, (c) color image inversion, (d) vessel lumen mask, (e) vessel internal wall border, (f) internal diameter and vessel angle detection, (g) rotated lumen vessel mask.

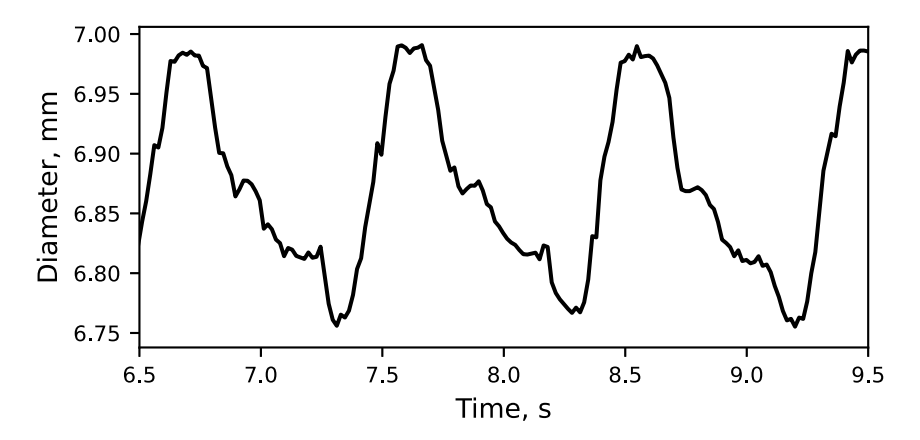


Fig. 8. Phantom diameter changes in time based on ultrasound image analysis.

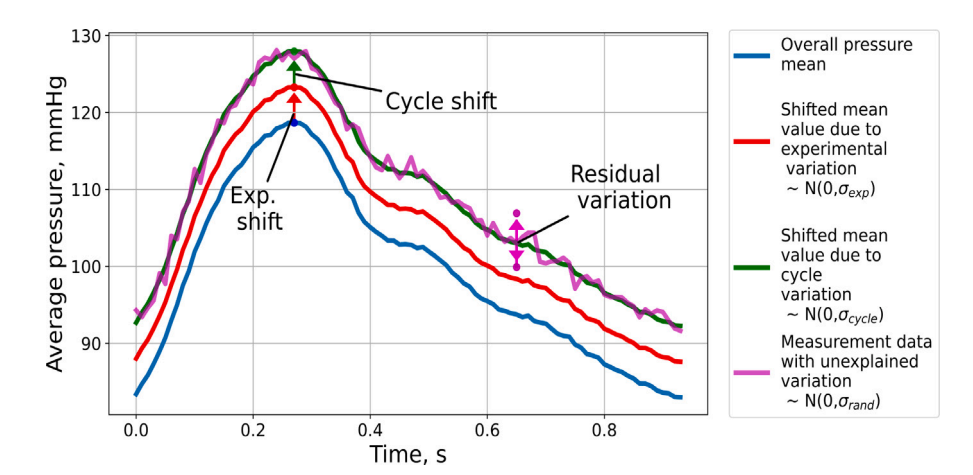


Fig. 9. Conceptual visualization of shifts in mean value due to experimental and cycle effects as well as random unexplained variance.

will tend to be shifted similarly on average, but individual cycles will vary around this shifted mean cycle. Finally, at an arbitrary time point, noise and sensor error result in residual variations in the measured data.

To evaluate the statistical significance of experiment-to-experiment and cycle-to-cycle variation, a series of models with varying complexity were compared. The analyses were conducted using the R programming language (R 4.2.0) and the lme4 package (version 1.1.30) [38]. To simplify the presentation we focus on a single pressure transducer, but the same approach was applied for all pressure transducers, flow meters and cameras. Let p_{ijk} denote the measured value of pressure at position i in the kth cycle from the jth experiment. The residuals ϵ_{ijk} are assumed to be independently, identically normally distributed with zero mean and standard deviation σ_e . First, an ordinary linear regression model (Null) is fit to the data

$$p_{ijk} = \mu_i + \epsilon_{ijk} \tag{2}$$

where μ_i is the mean value of pressure at position i of the cycle. The first mixed effects model (Exp. Effect) is

$$p_{ijk} = \mu_i + \tau_j + \epsilon_{ijk} \tag{3}$$

which introduces the shift τ_j for experiment j. Finally, the nested cycle effect model

$$p_{ijk} = \mu_i + \tau_j + \alpha_{k(j)} + \epsilon_{ijk} \tag{4}$$

additionally introduces the shift $\alpha_{k(j)}$ for cycle k of experiment j. Note that τ_j and $\alpha_{k(j)}$ are assumed to be independently, identically normally distributed with standard deviations σ_{exp} and σ_{cycle} respectively.

Likelihood-ratios [39] and information criteria [40] were used to assess if the variance in the data actually could be better attributed

Table 1
Reported values of model performance metrics (AIC, BIC) and likelihood-ratio tests.
The bottom row of Table 1 shows the value in comparison to the previous model. The likelihood-ratio tests were in favor of existence of grouping effects, giving p_{value} ≈ 0. Further, information criteria (Akaike Information Criterion, AIC, and Bayesian

Information Criterion, BIC [40]) also indicate the superiority of (4).

 Test\Model
 Null model
 Exp effect
 Nested cycle effect

 AIC
 277 245.8
 278 164.1
 253 098.6

 BIC
 257 486.4
 258 414
 254 035.7

 LRT
 x
 p < 0.001 p < 0.001

to grouping effects than residual variation (Table 1). Both assessments show that (4) better fits and explains the data than (2) or (3), and we consequently focus on the results for (4) in the following analysis.

To characterize the reproducibility of the shape of each sensor's waveform, a 95% confidence interval (CI) for μ_i was computed, while a 95% prediction interval (PI) for the mean of a new cycle, $\mu_i + \alpha_{k(j)}$, was computed to characterize the stability of the waveform level within a given experiment [28]. The CIs were obtained using the reported standard errors of the estimated fixed effects obtained from the model fit and using the formula [41]:

$$\hat{\mu}_i \pm z_{1-\frac{\alpha}{2}} \sqrt{\text{SE}(\hat{\mu}_i)} \tag{5}$$

for the CI of the mean cycle and

$$\hat{\mu}_i \pm z_{1-\frac{\alpha}{2}} \sqrt{\text{SE}(\hat{\mu}_i) + \hat{\sigma}_{cyc}}$$
 (6)

for the PI for a new cycle mean. SE denotes the standard error of an estimated parameter, and $z_{1-\frac{\alpha}{2}}$ is the $100\times(1-\frac{\alpha}{2})^{th}$ quantile of the Standard Normal Distribution (here $\alpha=2.5$ to get 95% confidence [28]).

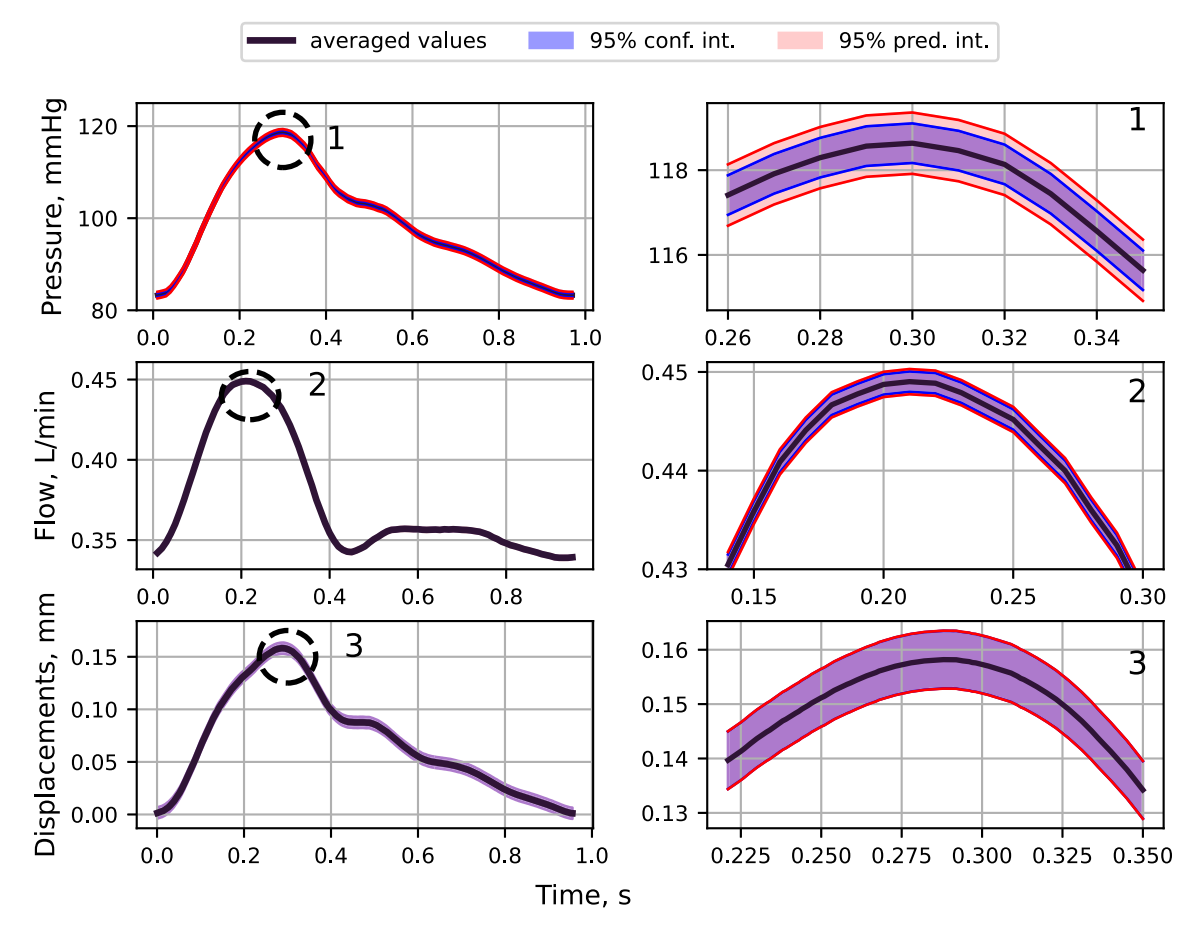


Fig. 10. Asymptotic prediction and confidence intervals for the models fitted to pressure, flow and displacement data in Case B. The left panels show the full waveform. The regions marked by dashed circles in the left panels are shown at a higher zoom in the right panels.

The maximum CI and PI widths, and the estimates $\hat{\sigma}_{exp}$, $\hat{\sigma}_{cyc}$ and $\hat{\sigma}_{resid}$ are reported for all equipment and cases in Table 2. The CI and PI for the full waveforms are shown in Fig. 10 for pressure transducer p1, the inlet flowmeter, and the VEO camera in case B. The widths are 0.942 mmHg and 1.476 mmHg for CI and PI respectively, while the estimated standard deviations are 0.623 mmHg, 0.282 mmHg and 1.026 mmHg for experiment, cycle and residual variation respectively. The values for the flow waveform were 2.08E-03, 2.61E-03, 9.59E-04, 3.87E-04 and 6.77E-03 L/min, and for the VEO camera 6.10E-03, 6.22E-03, 2.10E-03, 3.05E-04, 4.81E-03 mm. The magnitudes are similar across the transducers and cases with the exception of case C for which for nearly all sensors have the highest $\hat{\sigma}_{exp}$. The flow meters have higher values in case C compared to cases A and B, while $\hat{\sigma}_{exp}$ is highest for case D.

In general the widths of both PIs and CIs are narrow and confirm that the experimental procedure is reproducible and consistent. The residual variation tends to be larger than the experiment-to-experiment or cycle-to-cycle variation and suggests that high frequency noise sources are more significant than systematic variations between experiments; however, even the estimated standard deviations corresponding to these noise sources are very low compared to the mean values. While the experiment-to-experiment variation is larger in Case C compared to other estimates, some variability is to be expected in estimates of σ_{exp} as there are only 7 experiments in each case.

The residuals of the fitted statistical model were analyzed to identify if the assumptions of independence and normality are violated. The observed residuals are defined as the difference between the predicted and measured values given in terms of (4) as

$$\hat{\epsilon}_{ijk} = p_{ijk} - \hat{\mu}_i - \hat{\tau}_j - \hat{\alpha}_{k(j)}. \tag{7}$$

A Quantile–Quantile (QQ) plot [28], distribution fits [42], and a residuals-vs-cycle-time plot were used to assess the normality and independence of residuals [43]. In the QQ-plot (Fig. 11 right) the tails of the curve stray from the Standard Normal quantiles indicating a non-normal distribution of residuals. Moreover, the fitted normal distribution has a broader peak and smaller tails compared with the estimated residuals (Fig. 11 left). A mixture of two normal distributions ($N_1(0.027, 0.733)$) and $N_2(-0.112, 1.778)$) [44] seems to fit the residuals well, and the plot of residuals vs cycle time (Fig. 12) reveals that the first half of the cycle tends to have more widely distributed residuals than the second half which is consistent with such a distribution. As the residuals seem to be distributed symmetrically, the statistical inferences based on the linear mixed effects model are likely unaffected [45].

To corroborate the interpretation of the residuals, ϵ_{ijk} , as sensor error, the distribution of the residuals was compared across equipment and cases. It is expected that the same type of sensors will produce similar distributions of residuals. The results are shown in a form of a probability density plot Fig. 13 match this expectation as the residuals are mostly clustered around 0 and their shape is consistent across cases.

An example of simultaneous displacement values from both cameras are presented in Fig. 14 with the uncertainties estimated by the mixed model analysis. Displacement values from both cameras are generally close to each other and mostly lie either within the range corresponding to the calculated uncertainties, which demonstrates that the results are very similar across cameras and that the phantom deforms similarly along its principal axes.

6. Ultrasound image measurements results

To assess the performance of the US system two procedures were conducted. First, the resolution, accuracy, and precision of the US

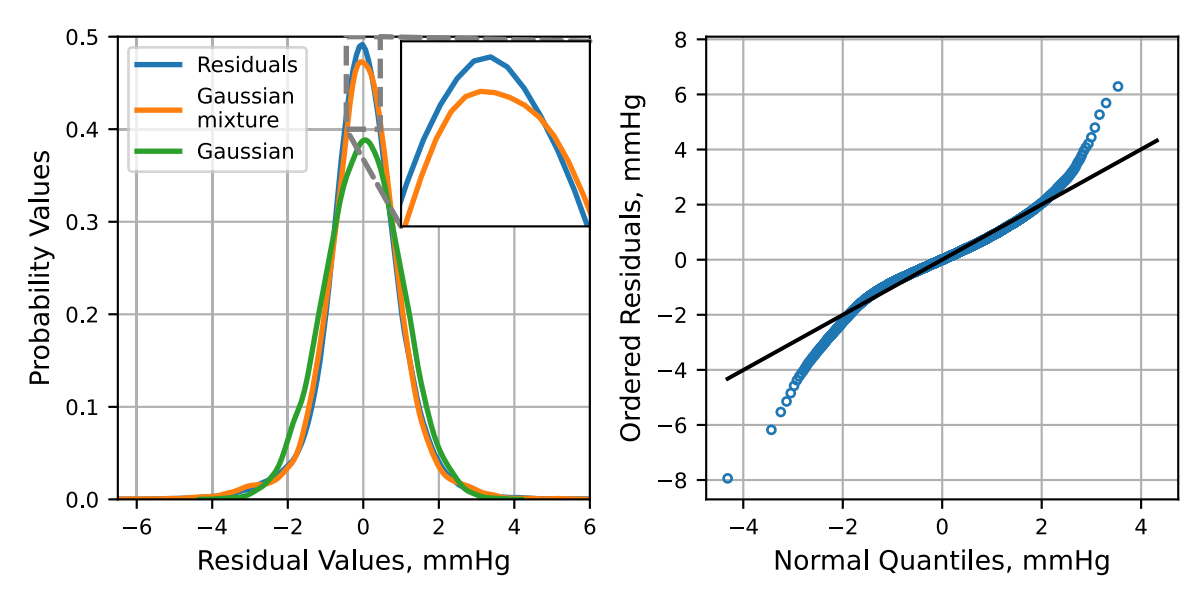


Fig. 11. Fitted residual distributions are shown on the left with an inset showing the details of the peak. A QQ-Plot for the nested model residuals is given on the right, indicating in the tails that the residuals stray very far from theoretical quantiles. Gaussian mixture fit captures the overall distribution pretty well, except at the very peak (zoomed).

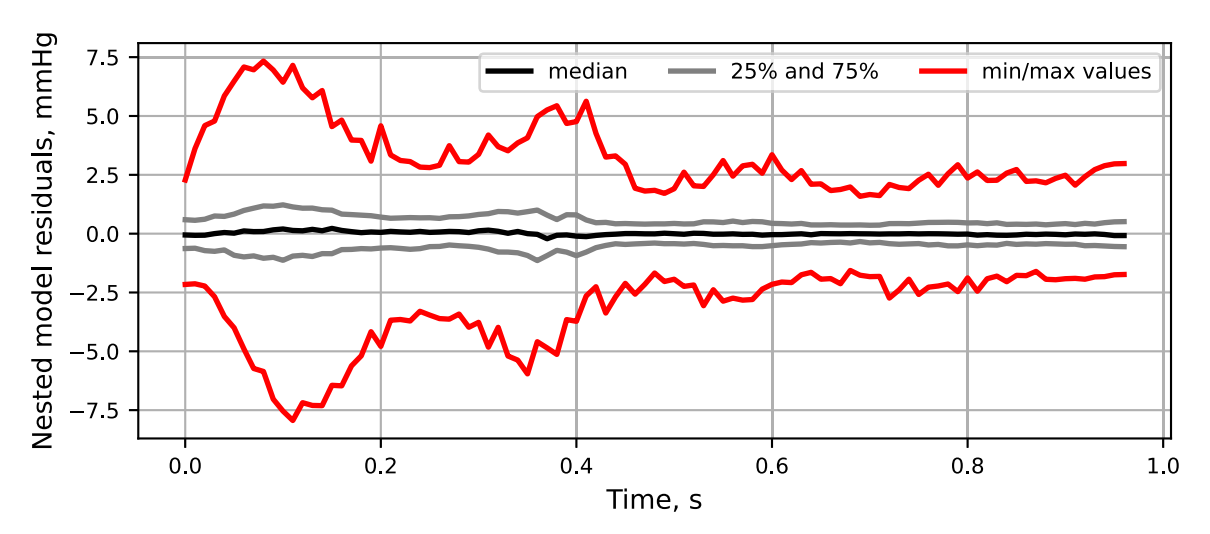


Fig. 12. Selected quantiles of residuals of pressure for a nested model plotted versus time.

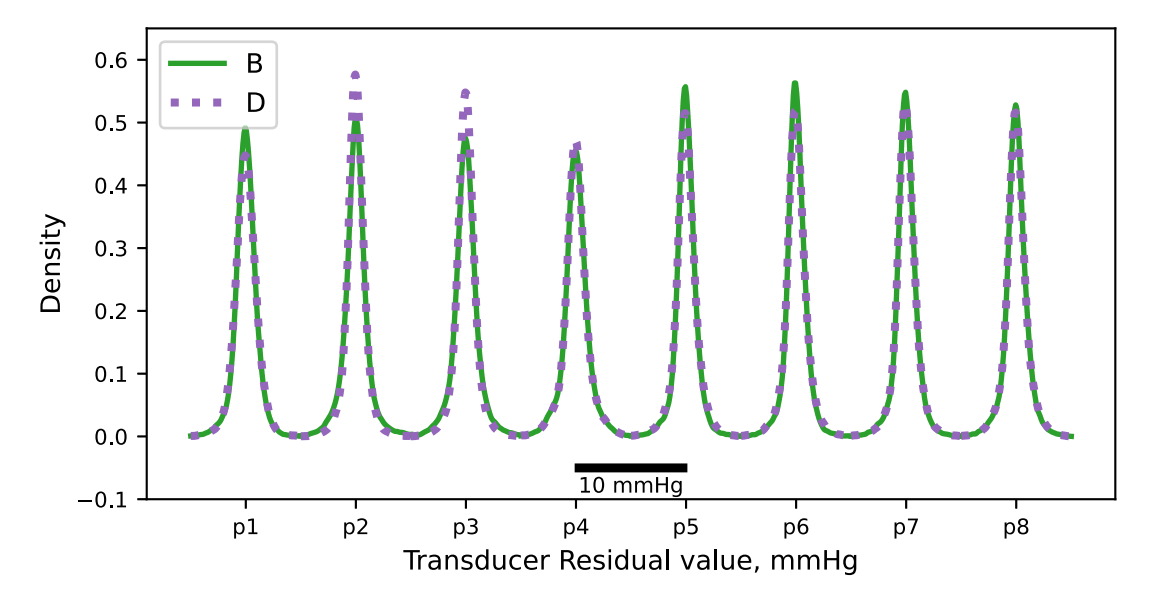


Fig. 13. Plot of the distribution of residuals across all pressure transducers for two cases (Case B: 120/80 and Case D: 140/100).

Table 2
Summary of estimated cycle, experimental and residual standard deviations, along with maximum width of prediction and confidence intervals (for all cases).

| Equipment | Case A: 110/70 | | | | | Case B: 120/80 | | | | |
|--|--|---|---|---|---|--|---|---|---|---|
| | CI max width | PI max width | $\hat{\sigma}_{exp}$ | $\hat{\sigma}_{cyc}$ | $\hat{\sigma}_{resid}$ | CI max width | PI max width | $\hat{\sigma}_{exp}$ | $\hat{\sigma}_{cyc}$ | $\hat{\sigma}_{resid}$ |
| p1, mmHg | 0.622 | 1.530 | 0.409 | 0.349 | 0.953 | 0.942 | 1.476 | 0.623 | 0.282 | 1.026 |
| p2, mmHg | 0.625 | 1.514 | 0.411 | 0.344 | 0.962 | 0.893 | 1.423 | 0.587 | 0.275 | 1.145 |
| p3, mmHg | 0.643 | 1.515 | 0.421 | 0.342 | 1.089 | 0.964 | 1.469 | 0.635 | 0.275 | 1.163 |
| p4, mmHg | 0.649 | 1.511 | 0.424 | 0.340 | 1.108 | 1.011 | 1.502 | 0.667 | 0.276 | 1.155 |
| p5, mmHg | 0.652 | 1.528 | 0.430 | 0.345 | 0.860 | 0.984 | 1.500 | 0.652 | 0.281 | 0.951 |
| p6, mmHg | 0.671 | 1.546 | 0.442 | 0.347 | 0.912 | 1.014 | 1.526 | 0.672 | 0.283 | 0.937 |
| p7, mmHg | 0.658 | 1.527 | 0.433 | 0.344 | 0.938 | 0.971 | 1.493 | 0.643 | 0.281 | 0.970 |
| p8, mmHg | 0.648 | 1.520 | 0.426 | 0.343 | 1.007 | 0.940 | 1.472 | 0.621 | 0.281 | 1.008 |
| EH1, L/min | 1.817E-03 | 1.836E-03 | 7.109E-04 | 5.322E-04 | 1.147E-02 | 2.079E-03 | 2.609E-03 | 9.591E-04 | 3.874E-04 | 6.774E-03 |
| EH2, L/min | 1.854E-03 | 1.873E-03 | 8.109E-04 | 1.144E-09 | 1.010E-02 | 2.079E-03 | 2.609E-03 | 9.591E-04 | 3.874E-04 | 6.774E-03 |
| MIRO, mm | 2.421E-02 | 2.448E-02 | 5.608E-03 | 9.247E-04 | 2.596E-02 | 5.113E-03 | 5.316E-03 | 1.497E-03 | 3.682E-04 | 5.305E-03 |
| VEO, mm | 1.631E-02 | 1.660E-02 | 5.641E-03 | 7.844E-04 | 1.829E-02 | 6.098E-03 | 6.217E-03 | 2.975E-03 | 3.048E-04 | 4.812E-03 |
| | Case C: 130/90 | | | | | Case D: 140/100 | | | | |
| Equipment | Case C: 130/90 | | | | | Case D: 140/10 | 0 | | | |
| Equipment | Case C: 130/90 CI max width | PI max width | $\hat{\sigma}_{exp}$ | $\hat{\sigma}_{cyc}$ | $\hat{\sigma}_{resid}$ | Case D: 140/10 CI max width | O PI max width | $\hat{\sigma}_{exp}$ | $\hat{\sigma}_{cyc}$ | $\hat{\sigma}_{resid}$ |
| Equipment p1, mmHg | | | $\hat{\sigma}_{exp}$ 3.056 | $\hat{\sigma}_{cyc}$ | $\hat{\sigma}_{resid}$ 1.373 | | - | $\hat{\sigma}_{exp}$ 0.343 | $\hat{\sigma}_{cyc}$ 0.369 | $\hat{\sigma}_{resid}$ 1.056 |
| | CI max width | PI max width | | | | CI max width | PI max width | | | |
| p1, mmHg | CI max width | PI max width | 3.056 | 0.346 | 1.373 | CI max width | PI max width | 0.343 | 0.369 | 1.056 |
| p1, mmHg p2, mmHg | CI max width 4.577 4.562 | PI max width 4.826 4.810 | 3.056 3.046 | 0.346 0.345 | 1.373 1.443 | CI max width 0.497 0.481 | PI max width 1.557 1.557 | 0.343 0.335 | 0.369 0.370 | 1.056 0.889 |
| p1, mmHg p2, mmHg p3, mmHg | CI max width 4.577 4.562 4.583 | PI max width 4.826 4.810 4.828 | 3.056 3.046 3.060 | 0.346 0.345 0.342 | 1.373 1.443 1.506 | CI max width 0.497 0.481 0.471 | PI max width 1.557 1.557 1.556 | 0.343 0.335 0.327 | 0.369 0.370 0.370 | 1.056 0.889 0.943 |
| p1, mmHg p2, mmHg p3, mmHg p4, mmHg | CI max width 4.577 4.562 4.583 4.581 | PI max width 4.826 4.810 4.828 4.825 | 3.056 3.046 3.060 3.058 | 0.346 0.345 0.342 0.342 | 1.373 1.443 1.506 1.493 | CI max width 0.497 0.481 0.471 0.475 | PI max width 1.557 1.557 1.556 1.534 | 0.343 0.335 0.327 0.326 | 0.369 0.370 0.370 0.364 | 1.056 0.889 0.943 1.137 |
| p1, mmHg p2, mmHg p3, mmHg p4, mmHg p5, mmHg | CI max width 4.577 4.562 4.583 4.581 4.569 | PI max width 4.826 4.810 4.828 4.825 4.822 | 3.056 3.046 3.060 3.058 3.051 | 0.346 0.345 0.342 0.342 0.349 | 1.373 1.443 1.506 1.493 1.301 | CI max width 0.497 0.481 0.471 0.475 0.459 | PI max width 1.557 1.557 1.556 1.534 1.518 | 0.343 0.335 0.327 0.326 0.316 | 0.369 0.370 0.370 0.364 0.361 | 1.056 0.889 0.943 1.137 1.042 |
| p1, mmHg p2, mmHg p3, mmHg p4, mmHg p5, mmHg | CI max width 4.577 4.562 4.583 4.581 4.569 4.593 | PI max width 4.826 4.810 4.828 4.825 4.825 4.846 | 3.056 3.046 3.060 3.058 3.051 3.067 | 0.346 0.345 0.342 0.342 0.349 0.351 | 1.373 1.443 1.506 1.493 1.301 1.290 | CI max width 0.497 0.481 0.471 0.475 0.459 0.471 | PI max width 1.557 1.557 1.556 1.534 1.518 1.542 | 0.343 0.335 0.327 0.326 0.316 0.326 | 0.369 0.370 0.370 0.364 0.361 0.367 | 1.056 0.889 0.943 1.137 1.042 1.018 |
| p1, mmHg p2, mmHg p3, mmHg p4, mmHg p5, mmHg p6, mmHg p7, mmHg | CI max width 4.577 4.562 4.583 4.581 4.569 4.593 4.579 | PI max width 4.826 4.810 4.828 4.825 4.825 4.822 4.846 4.832 | 3.056 3.046 3.060 3.058 3.051 3.067 3.057 | 0.346 0.345 0.342 0.342 0.349 0.351 0.349 | 1.373 1.443 1.506 1.493 1.301 1.290 1.303 | CI max width 0.497 0.481 0.471 0.475 0.459 0.471 0.471 | PI max width 1.557 1.557 1.556 1.534 1.518 1.542 1.543 | 0.343 0.335 0.327 0.326 0.316 0.326 0.325 | 0.369 0.370 0.370 0.364 0.361 0.367 | 1.056 0.889 0.943 1.137 1.042 1.018 0.999 |
| p1, mmHg p2, mmHg p3, mmHg p4, mmHg p5, mmHg p6, mmHg p7, mmHg p8, mmHg | CI max width 4.577 4.562 4.583 4.581 4.569 4.593 4.579 4.566 | PI max width 4.826 4.810 4.828 4.825 4.822 4.846 4.832 4.816 | 3.056 3.046 3.060 3.058 3.051 3.067 3.057 3.049 | 0.346 0.345 0.342 0.342 0.349 0.351 0.349 0.347 | 1.373 1.443 1.506 1.493 1.301 1.290 1.303 1.305 | 0.497 0.481 0.471 0.475 0.459 0.471 0.471 0.471 | PI max width 1.557 1.557 1.556 1.534 1.518 1.542 1.543 1.550 | 0.343 0.335 0.327 0.326 0.316 0.326 0.325 0.341 | 0.369 0.370 0.370 0.364 0.361 0.367 0.367 | 1.056 0.889 0.943 1.137 1.042 1.018 0.999 1.031 |
| p1, mmHg p2, mmHg p3, mmHg p4, mmHg p5, mmHg p6, mmHg p7, mmHg p8, mmHg EH1, L/min | CI max width 4.577 4.562 4.583 4.581 4.569 4.593 4.579 4.566 1.178E-02 | PI max width 4.826 4.810 4.828 4.825 4.822 4.846 4.832 4.816 1.190E-02 | 3.056 3.046 3.060 3.058 3.051 3.067 3.057 3.049 7.089E-03 | 0.346 0.345 0.342 0.342 0.349 0.351 0.349 0.347 0.000E+00 | 1.373 1.443 1.506 1.493 1.301 1.290 1.303 1.305 1.356E-02 | CI max width 0.497 0.481 0.471 0.475 0.459 0.471 0.471 0.493 3.196E-02 | PI max width 1.557 1.557 1.556 1.534 1.518 1.542 1.543 1.550 3.228E-02 | 0.343 0.335 0.327 0.326 0.316 0.326 0.325 0.341 2.123E-02 | 0.369 0.370 0.370 0.364 0.361 0.367 0.367 0.367 2.309E-03 | 1.056 0.889 0.943 1.137 1.042 1.018 0.999 1.031 2.053E-02 |

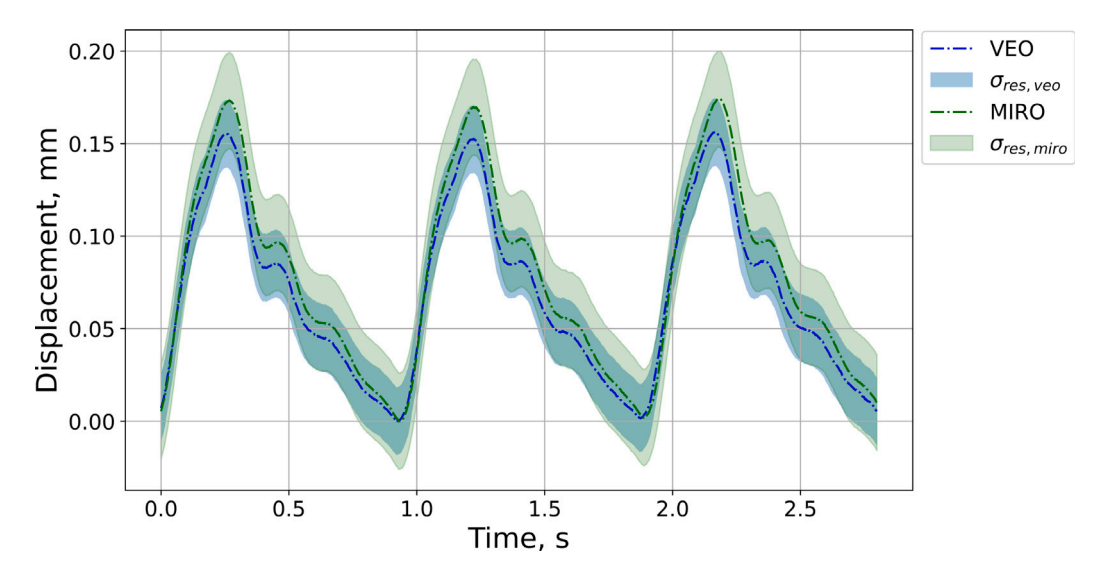


Fig. 14. Comparison of displacements recorded by both cameras with uncertainty represented by overlaid shaded areas. In both cases the uncertainty is characterized as $d_{rel,cam} \pm \hat{\sigma}_{res,cam}$.

system was evaluated with a specially built phantom. Second, the MIRO (top view) camera was replaced with an US probe and the same experimental conditions as used for the dual camera cases were repeated to collect displacement data simultaneously with VEO and US for comparison.

For the applied settings of ultrasound system the pixel size is 0.025 mm, however, the observed resolution was lower. For ultrasound systems, the image resolution depends on many factors like depths, ultrasound wave frequency, type of imaging tissues etc. For that reason, the determination of the functional resolution is not unequivocal [46]. The measured differences in the phantom diameter between diastole and systole are minimal — around 0.2 mm. Therefore, besides the spatial resolution, the system's precision and accuracy for the measurement conditions were determined. The system's spatial resolution was defined as a minimum distance between two points (lines) for which

these points (lines) are still distinguishable. The accuracy is described as the apparent diameter of a point object imaged by the system; that is the Point Spread Function. Precision, on the other hand, defines the scatter of the results [47,48]. For ultrasound imaging, the precision is determined by measuring how exactly the moving point can be tracked in the image. Using this definition, the accuracy describes the exactness with which the absolute size or position of the object can be measured, while the precision describes how exactly the displacement of the same point can be measured.

To determine the ultrasound system's resolution, accuracy, and precision, a wire-based phantom was developed. This consists of a fluorocarbon monofilament fishline (0.1 mm diameter) used to create the physical line and LEGO bricks to create the frame. LEGO bricks are a common material for creating phantoms for the purpose of calibrating and investigating ultrasound systems [49,50]. The phantom has been

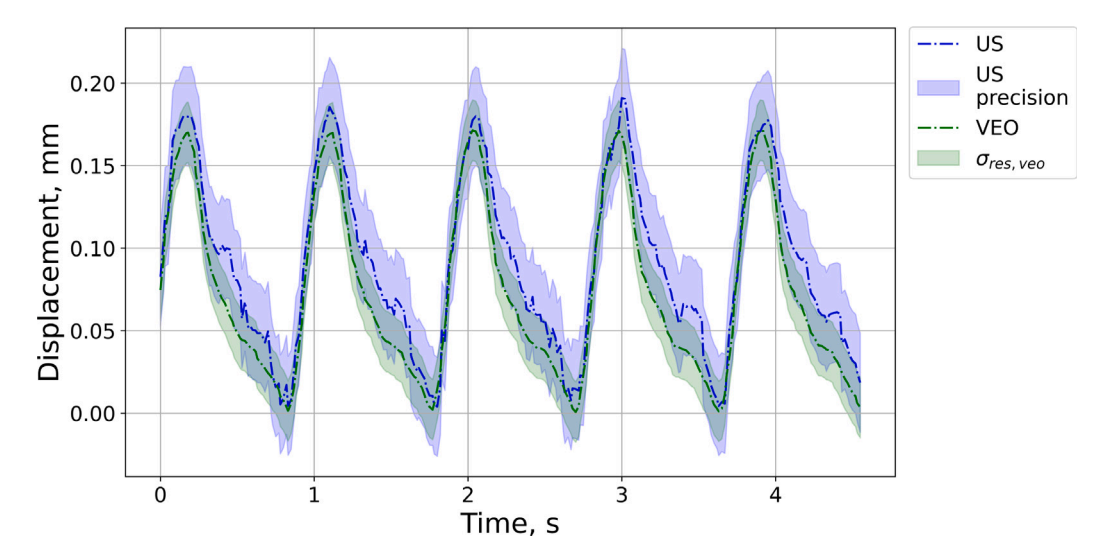


Fig. 15. Comparison of displacements recorded by the US and VEO camera. VEO's uncertainty is characterized as $d_{rel,veo} \pm \hat{\sigma}_{resid,veo}$, while US system's uncertainty is characterized $d_{rel,us} \pm precision$.

constructed so that the two lines intersect. The position and angle of one line can be changed relative to another. This allows precise adjustment of the distance between the lines. All measurements were performed on ultrasound images recorded under the same measurement conditions as the experiments. For measuring distances the ultrasound system's built-in tools were used. The resolution was determined as the minimal distance between two lines such that both fishlines are independently visible in the ultrasound image. The measured resolution was 0.4 mm. Accuracy was determined as the apparent diameter of the fishline in an ultrasound image was measured. The accuracy defined in such a way was 0.4 mm. To determine the precision, the minimal observable shift distance between two positions of the same fishline was measured. The measured distance was 0.03 mm.

While the fishline based measurements are useful to characterize the US system, a direct comparison of measured displacements from the phantom is more representative of how US would perform for the application of interest. Fig. 15 shows the displacements measured by US and by the side camera, VEO, for case B. It can be seen that the magnitude of the displacement is almost the same for both devices. Curves seem to overlap very well. Moreover, the measured US values lie comfortably within the calculated camera's uncertainty, indicating that a US can be used to detect the displacements of a material with high accuracy.

This is further corroborated by numerical data in Table 3 which reports the average difference of point-wise, \bar{A}_{PW} , cycle-average \bar{A}_{CW} , diastolic, \bar{A}_{dias} , and systolic, \bar{A}_{sys} , displacements between the cameras (VEO vs MIRO) or between the camera and ultrasound (VEO vs US). The difference is computed as $A_{[\]}=d_{[\], \text{VEO}}-d_{[\], Y}$ where Y is one of MIRO or US and $d_{[\]}$ denotes the displacement compared. For \bar{A}_{CW} , \bar{A}_{dias} and \bar{A}_{sys} the displacements are computed for each cycle then the differences between synchronized cycles are averaged. The averages includes all measurements across all pressure levels. In the table one can see that the differences are small, on the order of 10% of the measured values. The small magnitude of the differences is also apparent in Figs. 14 and 15 where the measurements are generally quite close. On average, both MIRO and US tend to produce larger displacement values than VEO, thus it seems that the phantom deforms more in the horizontal plane than in the vertical plane.

7. Discussion and conclusions

In this article we describe an experimental rig for carrying out pressure, flow, camera and ultrasound measurements of a phantom model of the left common carotid artery. We developed an in house control

Table 3 Numerical summary of averaged differences calculated between cameras (VEO vs. MIRO) or camera and ultrasound (VEO vs. US). The first column, $\bar{\Delta}_{PW}$, results from a point-wise comparison, the second, $\bar{\Delta}_{CW}$, results from comparison of cycle-average displacements, and the final two columns result from comparison of the diastolic, $\bar{\Delta}_{dias}$, and systolic, $\bar{\Delta}_{sys}$, displacements.

| Comparison\Type | $\bar{\Delta}_{PW}, \ \mathrm{mm}$ | $\bar{\Delta}_{CW}$, mm | $\bar{\Delta}_{dias}$, mm | $\bar{\Delta}_{sys}$, mm |
|-----------------|------------------------------------|--------------------------|----------------------------|---------------------------|
| VEO vs. US | -0.0188 | -0.0139 | -0.0067 | -0.0124 |
| VEO vs. MIRO | -0.0113 | -0.0010 | -0.0018 | -0.0219 |

application in LabVIEW and described the post-processing algorithms we employed to analyze the pressure, flow and image data resulting from a series of experiments over physiological ranges of pressures. A statistical analysis of measurement variability was carried out in order to characterize the uncertainties about the data for subsequent comparison with numerical models. Some of the measured data will serve as boundary conditions in the simulations, while the remaining data will be compared with the simulation results. Further the results of this analysis suggested that that the experiments were highly reproducible; σ_{exp} was less than 3.1 mmHg, 0.023 L/min, and 0.012 mm for pressure, flow and displacement respectively (see Table 2. The residual variation σ_{resid} seems consistent with high frequency noise from uncontrollable sources (environmental and equipment noise). Further, the deformation of the phantom was confirmed to be similar in two orthogonal planes by comparison of the displacements measured by cameras.

In addition to demonstrate the operational characteristics of the experimental rig, we assessed the performance of an ultrasound system for measuring the displacements of the phantom model of the artery. In comparison with the camera derived data, the ultrasound derived displacements exhibit good agreement (mean difference of 0.0113 mm), although slightly more deviation on average between ultrasound and camera than between the two cameras (see Table 3). The agreement of ultrasound derived displacements with optically measured results supports further use of ultrasound as a modality for characterizing the displacement of arterial walls. The experimental phantom and ultrasound measurement system have thus been confirmed to provide a reproducible experimental model for generating data for developing and testing new methods for non-invasive assessment of the common carotid artery.

CRediT authorship contribution statement

Aleksander Sinek: Visualization, Writing – original draft, Investigation, Software, Validation. Mateusz Mesek: Visualization, Writing – original draft. Marek Rojczyk: Writing – Review & editing, Investigation. Jan Juszczyk: Investigation, Visualization. Wojciech P. Adamczyk: Supervision, Methodology, Data curation, Conceptualization, Software. Jacob Sturdy: Supervision, Writing – review & editing, Validation, Software. Bartłomiej Melka: Investigation. Adam Golda: Formal analysis. Michał Nowok: Formal analysis. Ziemowit Ostrowski: Writing – review & editing, Formal analysis. Ryszard Białecki: Supervision, Writing – review & editing, Project administration.

Declaration of competing interest

The authors declare the following financial interests/personal relationships which may be considered as potential competing interests: Ryszard Bialecki reports financial support was provided by National Science Centre Poland. Wojciech Adamczyk reports financial support was provided by National Science Centre Poland.

Data availability

Data will be made available on request.

Acknowledgments

The research leading to these results is funded from the Norwegian Financial Mechanism 2014-2021 operated by the National Science Center, PL (NCN) within GRIEG programme under grant# UMO-2019/34/H/ST8/00624, project non-invasivE iN-vivo assessmenT Human aRtery wALls (ENTHRAL) [18] and by the National Science Center within OPUS scheme under contract 2017/27/B/ST8/01046 and partially by the National Science Center within the OPUS scheme under contract 2018/31/B/ST8/02201 and Ministry of Education and Science (Poland) under statutory research funds of the Faculty of Energy and Environmental Engineering of SUT under contract BK-252/RIE6/2023 08/060/BK 23/1096.

References

- [1] C.W. Tsao, A.W. Aday, Z.I. Almarzooq, A. Alonso, A.Z. Beaton, M.S. Bittencourt, A.K. Boehme, A.E. Buxton, A.P. Carson, Y. Commodore-Mensah, et al., Heart disease and stroke statistics—2022 update: a report from the American Heart Association, Circulation 145 (8) (2022) e153–e639.
- [2] A. Bustamante, T. Garcia-Berrocoso, N. Rodriguez, V. Llombart, M. Ribo, C. Molina, J. Montaner, Ischemic stroke outcome: A review of the influence of post-stroke complications within the different scenarios of stroke care, Eur. J. Internal Med. 29 (2016) 9–21.
- [3] J.A. Chirinos, P. Segers, T. Hughes, R. Townsend, Large-artery stiffness in health and disease: JACC state-of-the-art review, J. Am. Coll. Cardiol. 74 (9) (2019) 1237–1263.
- [4] S. Oktamuliani, N. Kanno, M. Maeda, K. Hasegawa, Y. Saijo, Validation of echodynamography in comparison with particle-image velocimetry, Ultrason. Imaging 41 (2019) 336–352, http://dx.doi.org/10.1177/0161734619879859, URL http://journals.sagepub.com/doi/10.1177/0161734619879859.
- [5] N. Mirvakili, G.D. Labbio, W. Saleh, L. Kadem, Flow characteristics in a model of a left ventricle in the presence of a dysfunctional mitral mechanical heart valve, J. Vis. 23 (2020) 1–8, http://dx.doi.org/10.1007/s12650-019-00611-3, URL http://link.springer.com/10.1007/s12650-019-00611-3.
- [6] Y. Li, D.I. Verrelli, W. Yang, Y. Qian, W. Chong, A pilot validation of CFD model results against PIV observations of haemodynamics in intracranial aneurysms treated with flow-diverting stents, J. Biomech. 100 (2020) 109590, http://dx. doi.org/10.1016/J.JBIOMECH.2019.109590.
- [7] M. Jeyhani, S. Shahriari, M. Labrosse, Experimental investigation of left ventricular flow patterns after percutaneous edge-to-edge mitral valve repair, Artif. Organs 42 (2018) 516–524, http://dx.doi.org/10.1111/aor.13020, URL http://doi.wilev.com/10.1111/aor.13020.
- [8] C. Seaman, A.G. Akingba, P. Sucosky, Steady flow hemodynamic and energy loss measurements in normal and simulated calcified tricuspid and bicuspid aortic valves, J. Biomech. Eng. 136 (2014) http://dx.doi.org/10.1115/1.4026575.

[9] P. Segers, E.R. Rietzschel, J.A. Chirinos, How to measure arterial stiffness in humans, Arterioscler. Thromb. Vasc. Biol. 40 (5) (2020) 1034–1043.

- [10] A. Gotschy, W.R. Bauer, P. Winter, P. Nordbeck, E. Rommel, P.M. Jakob, V. Herold, Local versus global aortic pulse wave velocity in early atherosclerosis: An animal study in ApoE-/-mice using ultrahigh field MRI, PLoS One 12 (2) (2017) e0171603
- [11] T. Pereira, C. Correia, J. Cardoso, Novel methods for pulse wave velocity measurement, J. Med. Biol. Eng. 35 (5) (2015) 555–565.
- [12] B. Williams, G. Mancia, W. Spiering, E. Agabiti Rosei, M. Azizi, M. Burnier, D.L. Clement, A. Coca, G. De Simone, A. Dominiczak, et al., 2018 ESC/ESH guidelines for the management of arterial hypertension: The Task Force for the management of arterial hypertension of the European Society of Cardiology (ESC) and the European Society of Hypertension (ESH), Eur. Heart J. 39 (33) (2018) 3021–3104
- [13] C.-J. Tang, P.-Y. Lee, Y.-H. Chuang, C.-C. Huang, Measurement of local pulse wave velocity for carotid artery by using an ultrasound-based method, Ultrasonics 102 (2020) 106064.
- [14] A. Christ, D. Barowsky, M. Gekle, O. Thews, A hydraulic model of cardiovascular physiology and pathophysiology embedded into a computer-based teaching system for student training in laboratory courses, Adv. Physiol. Educ. (2020).
- [15] J. Calabia, P. Torguet, M. Garcia, I. Garcia, N. Martin, B. Guasch, D. Faur, M. Vallés, Doppler ultrasound in the measurement of pulse wave velocity: agreement with the Complior method, Cardiovasc. Ultrasound 9 (1) (2011) 1–6.
- [16] K.V. Ramnarine, T. Anderson, P.R. Hoskins, Construction and geometric stability of physiological flow rate wall-less stenosis phantoms, Ultrasound Med. Biol. 27 (2) (2001) 245–250.
- [17] M. Pankow, B. Justusson, A.M. Waas, Three-dimensional digital image correlation technique using single high-speed camera for measuring large out-of-plane displacements at high framing rates, Appl. Opt. 49 (17) (2010) 3418–3427.
- [18] Non-invasive in-vivo assessment of the stiffness of human artery walls, 2022, https://enthral.pl/.
- [19] M.S. Islam, T. Lehtimäki, M. Juonala, M. Kähönen, N. Hutri-Kähönen, K. Kainulainen, H. Miettinen, L. Taittonen, K. Kontula, J.S. Viikari, O.T. Raitakari, Polymorphism of the angiotensin-converting enzyme (ACE) and angiotesinogen (AGT) genes and their associations with blood pressure and carotid artery intima media thickness among healthy Finnish young adults—the Cardiovascular Risk in Young Finns Study, Atherosclerosis 188 (2) (2006) 316–322, http://dx.doi.org/10.1016/j.atherosclerosis.2005.11.008, URL https://www.sciencedirect.com/science/article/pii/S0021915005007343.
- [20] Harvard apparatus, 2022, https://www.harvardapparatus.com/, accessed: 2022-10-17.
- [21] Endress Hauser, 2022, https://www.endress.com/en, Accessed: 2022-10-17.
- [22] Phantom, 2022, https://www.phantomhighspeed.com/, Accessed: 2022-10-17.
- [23] Irix, 2022, https://irixlens.com/, Accessed: 2022-10-17.
- [24] Kobold manual, 2021, https://www.kobold.com/uploads/files/s4gbm_drs.pdf#:~:text=to%20Request%20Quote-,The%20Compact%20Transducer% 20Amplifier%20(CTA)%20is%20a%20DC%20bridge-,transducer%20must% 20be%20ordered%20together.
- [25] CTAs manual, 2022, https://www.harvardapparatus.com/compact-transducer-amplifier.html#:~:text=to%20Request%20Quote-, The%20Compact%20Transducer%20Amplifier%20(CTA)%20is%20a%20DC%20bridge-, transducer%20must%20be%20ordered%20together.
- [26] H. Liu, S. Shah, W. Jiang, On-line outlier detection and data cleaning, Comput. Chem. Eng. 28 (9) (2004) 1635–1647.
- [27] M. Vlachos, P. Yu, V. Castelli, On periodicity detection and structural periodic similarity, in: Proceedings of the 2005 SIAM International Conference on Data Mining, SIAM, 2005, pp. 449–460.
- [28] J.L. Devore, Probability and Statistics for Engineering and the Sciences, Cengage learning, 2011.
- [29] G. Bradski, The OpenCV library, Dr. Dobb's J. Softw. Tools (2000).
- [30] C.R. Harris, K.J. Millman, S.J. van der Walt, R. Gommers, P. Virtanen, D. Cournapeau, E. Wieser, J. Taylor, S. Berg, N.J. Smith, R. Kern, M. Picus, S. Hoyer, M.H. van Kerkwijk, M. Brett, A. Haldane, J.F. del Río, M. Wiebe, P. Peterson, P. Gérard-Marchant, K. Sheppard, T. Reddy, W. Weckesser, H. Abbasi, C. Gohlke, T.E. Oliphant, Array programming with NumPy, Nature 585 (7825) (2020) 357–362, http://dx.doi.org/10.1038/s41586-020-2649-2.
- [31] P. Virtanen, R. Gommers, T.E. Oliphant, M. Haberland, T. Reddy, D. Cournapeau, E. Burovski, P. Peterson, W. Weckesser, J. Bright, S.J. van der Walt, M. Brett, J. Wilson, K.J. Millman, N. Mayorov, A.R.J. Nelson, E. Jones, R. Kern, E. Larson, C.J. Carey, İ. Polat, Y. Feng, E.W. Moore, J. VanderPlas, D. Laxalde, J. Perktold, R. Cimrman, I. Henriksen, E.A. Quintero, C.R. Harris, A.M. Archibald, A.H. Ribeiro, F. Pedregosa, P. van Mulbregt, SciPy 1.0 Contributors, SciPy 1.0: Fundamental algorithms for scientific computing in Python, Nature Methods 17 (2020) 261–272, http://dx.doi.org/10.1038/s41592-019-0686-2.
- [32] W. McKinney, et al., Data structures for statistical computing in python, in: Proceedings of the 9th Python in Science Conference, Vol. 445, Austin, TX, 2010, pp. 51–56.
- [33] C.A. Schneider, W.S. Rasband, K.W. Eliceiri, NIH Image to ImageJ: 25 years of image analysis, Nature Methods 9 (7) (2012) 671–675.

- [34] J. Canny, A computational approach to edge detection, IEEE Trans. Pattern Anal. Mach. Intell. (6) (1986) 679–698.
- [35] N. Otsu, Threshold selection method from gray-level histograms, IEEE Trans. Syst. Man Cybern. SMC-9 (1979) 62-66, http://dx.doi.org/10.1109/TSMC.1979. 4310076
- [36] I. Sobel, An isotropic 3x3 image gradient operator, in: Presentation at Stanford A.I. Project 1968, 2014.
- [37] R.O. Duda, P.E. Hart, Use of the Hough transformation to detect lines and curves in pictures, Commun. ACM 15 (1) (1972) 11–15.
- [38] D. Bates, M. Mächler, B. Bolker, S. Walker, Fitting linear mixed-effects models using lme4, J. Stat. Softw. 67 (1) (2015) 1–48, http://dx.doi.org/10.18637/jss. v067.i01.
- [39] K.-R. Koch, Parameter Estimation and Hypothesis Testing in Linear Models, Springer Science & Business Media, 1999.
- [40] S.I. Vrieze, Model selection and psychological theory: a discussion of the differences between the Akaike information criterion (AIC) and the Bayesian information criterion (BIC), Psychol. Methods 17 (2) (2012) 228.
- [41] B.G. Francq, D. Lin, W. Hoyer, Confidence, prediction, and tolerance in linear mixed models, Stat. Med. 38 (30) (2019) 5603–5622.
- [42] N. Commeau, E. Parent, M.-L. Delignette-Muller, M. Cornu, Fitting a lognormal distribution to enumeration and absence/presence data, Int. J. Food Microbiol. 155 (3) (2012) 146–152.
- [43] A. Loy, H. Hofmann, D. Cook, Model choice and diagnostics for linear mixedeffects models using statistics on street corners, J. Comput. Graph. Statist. 26 (3) (2017) 478–492.

[44] D.A. Reynolds, Gaussian mixture models, in: Encyclopedia of Biometrics, Vol. 741, 2009, (659–663).

Measurement 216 (2023) 112904

- [45] C.J. Maas, J.J. Hox, The influence of violations of assumptions on multilevel parameter estimates and their standard errors, Comput. Statist. Data Anal. 46 (3) (2004) 427–440.
- [46] A. Ng, J. Swanevelder, Resolution in ultrasound imaging, Contin. Educ. Anaesth. Crit. Care Pain 11 (2011) 186–192, http://dx.doi.org/10.1093/BJACEACCP/ MKR030, URL https://academic.oup.com/bjaed/article/11/5/186/283004.
- [47] JCGM, Evaluation of measurement data-Guide to the expression of uncertainty in measurement Évaluation des données de mesure-Guide pour l'expression de l'incertitude de mesure, 2008, URL www.bipm.org.
- [48] V. Hingot, A. Chavignon, B. Heiles, O. Couture, Measuring image resolution in ultrasound localization microscopy, IEEE Trans. Med. Imaging 40 (2021) 3812–3819, http://dx.doi.org/10.1109/TMI.2021.3097150.
- [49] R. Walsh, M. Soehl, A. Rankin, A. Lasso, G. Fichtinger, Design of a tracked ultrasound calibration phantom made of lego bricks, in: Medical Imaging 2014: Image-Guided Procedures, Robotic Interventions, and Modeling, Vol. 9036, SPIE, 2014, pp. 606–612.
- [50] Y. Xiao, C.X.B. Yan, S. Drouin, D. De Nigris, A. Kochanowska, D.L. Collins, User-friendly freehand ultrasound calibration using Lego bricks and automatic registration, Int. J. Comput. Assist. Radiol. Surg. 11 (9) (2016) 1703–1711.